Determination of layer-resolved composition, magnetization, and electronic structure of an Fe/MgO tunnel junction by standing-wave core and valence photoemission

See-Hun Yang, Benjamin Balke, Christian Papp, Sven Döring, Ulf Berges, L. Plucinski, Carsten Westphal, Claus M. Schneider, Stuart S. P. Parkin, and Charles S. Fadley

Phys. Rev. B **84**, 184410 — Published 11 November 2011

DOI: 10.1103/PhysRevB.84.184410

Submitted as PRB BF11537

Determination of layer-resolved composition, magnetization and electronic structure of an Fe/MgO tunnel junction by standing-wave core and valence photoemission

See-Hun Yang[1†], Benjamin Balke[2,3]*, Christian Papp[2,3,#], Sven Döring[4], Ulf Berges[4], L. Plucinski[5], Carsten Westphal[4], Claus M. Schneider[5], Stuart S. P. Parkin[1], and Charles S. Fadley[2,3□]

[1]*IBM Almaden Research Center, San Jose, California 95120, USA*
[2]*Materials Sciences Division, Lawrence Berkeley National Laboratory, Berkeley, California 94720 USA*
[3]*Department of Physics, University of California Davis, Davis, California 95616, USA*
[4]*Experimentelle Physik 1-Technische Universität Dortmund, Otto-Hahn-Strasse 4, D-44221 Dortmund, Germany*
[5]*Peter Grünberg Institut, PGI-6, Forschungszentrum Jülich GmbH, D-52425 Jülich, Germany*

**Present address: Institut für Anorganische und Analytische Chemie, Johannes Gutenberg-Universität, 55099 Mainz, Germany*
[#]*Present address: Lehrstuhl für Physikalische Chemie II, Universität Erlangen-Nürnberg, Egerlandstr. 3, D-91058 Erlangen, Germany*

[†] Electronic address: seeyang@us.ibm.com
[□] Electronic address: chuckfadley@gmail.com

ABSTRACT

Spin dependent tunneling across a highly textured MgO insulating barrier has received much attention due to its potential applications in various spintronic devices. However, the interfacial magnetic and electronic structure of a prototypical realization of this in Fe/MgO/Fe and the effective band gap of the MgO layer are still under debate. In order to resolve these issues we have employed standing-wave excited core- and valence-photoemission, as well as core-level magnetic circular dichroism (MCD) in photoemission, to study the Fe/MgO interface with sub-nm depth resolution. For our synthetic procedure, we show that the Fe/MgO interface is linearly intermixed in composition over a length of ~ 8 Å (~ 4 monolayers) and that there is a magnetic dead layer ~2-3 Å thick. The unambiguous extraction of depth-resolved density of states (DOS) reveals that the interfacial layer composition is mostly metallic and non-magnetic FeO_x, with $x \cong 1$, which accounts for a smaller magnetoresistance compared to theoretical predictions. The formation of the magnetic dead layer (FeO) at the interface should also reduce the tunneling spin polarization.

The analysis of our data also shows a clear valence band edge of ultrathin MgO layer at ~3.5 eV below the Fermi level (E_F) that is very close to that of single crystal bulk MgO. An analysis that does not consider the interdiffused region separately exhibits the valence band edge for MgO layer ~1.3 eV below E_F, which is significantly closer to the MgO barrier height estimated from magnetotransport measurements, and further suggests that the Fe/MgO interdiffusion effectively reduces the MgO band gap.

PACS numbers: 85.75.Dd, 79.60.-i, 79.60.Dp, 79.20.Ls

I. INTRODUCTION

Magnetic tunnel junctions (MTJs) consisting of an insulating barrier sandwiched by two ferromagnets [1,2] are being intensively used as e.g. read heads in hard disk drives and MRAM. To extend their application further to logic devices, a greater on-off ratio, i.e., tunneling magnetoresistance (TMR) ratio is required. The TMR ratio is defined as $(R_{AP} - R_P)/R_P$ where R_P and R_{AP} are junction resistances in parallel and anti-parallel magnetic configurations of the two electrodes, respectively. MTJs with an amorphous Al_2O_3 barrier exhibit at most 80~90% TMR ratios [3,4], which correspond to ~55% tunneling spin polarization *P,* as estimated from the Julliere model: $\mathrm{TMR} = 2P^2/(1-P^2)$ [5]. Recently, a theoretical prediction of giant TMR ratios from a crystalline MgO barrier [6,7] has been realized in experiments at room temperature [8,9]. It is known from theory that the MgO crystalline barrier filters out one orientation of spins preferentially due to a selective transmission of specific wave function symmetries, and thus actively provides an even higher TMR ratio than what is calculated from the simple Julliere formula and the electrode spin polarization at the Fermi level. At present, the highest TMR ratio at room temperature has reached more than 600% by use of Co-Fe-B ferromagnetic electrodes along with a highly textured MgO(100) barrier. However, this value is still smaller than what the theories predict (>1000%), and in addition the barrier height of the MgO layer estimated from transport measurements is significantly lower than that of single crystals. It is thus still not clear how the MgO electronic structure is changed by being in contact with the Fe electrodes, and how different methods of synthesis might affect this. A number of experimental and theoretical studies have been carried out on this system [10-25] but the exact nature of the Fe/MgO interface is still unclear. Previous soft x-ray spin-resolved photoemission experiments on epitaxial MBE-grown MgO on Fe(001) show an oxide-free interface [26], but other studies have reached opposing conclusions concerning this aspect. Furthermore, spin-dependent

attenuation of particular Fe-related direct-transition photoemission features as MgO layers have been made thicker, has been observed [27].

In this paper, we report on the depth-resolved composition and magnetic and electronic structure of the Fe/MgO interface by combining x-ray standing wave (SW) excitation of photoelectrons with a wedge-shaped sample profile in what has been termed the SWEDGE method [28-31]. Such standing wave-excited photoemission is based on growing the sample as, or in our case, on top of, a synthetic multilayer mirror, and has been shown in several prior studies to be capable of deriving depth profiles of concentration [28,29,32], magnetization [29], densities of states [31], and interface crystal field effects [32], in several spintronic multilayer structures. The measurements combine both wedge scans and rocking curves around the 1st order multilayer Bragg angle, and are analyzed by fitting the data to x-ray optical simulations with variable geometric and electronic structure parameters [30-32].

II. EXPERIMENTAL

The x-ray standing wave generating multilayer (80 alternate bilayers of $MoSi_2$ and Si with 39.82 Å periodicity) was prepared with rf-sputtering in the Center for X-ray Optics, LBNL, the top layer being Si. The multilayer period of 39.82 Å that translates into a 39.82 Å SW period above the mirror in 1st-order Bragg reflection; the thinner Mo layer (11.5 Å, compared to 28.3 Å for Si), leads to its being mostly $MoSi_2$, and thus being more stable against elevated temperatures during sample growth. On top of this was grown an Fe wedge, a constant thickness MgO layer, and a final Al_2O_3 capping layer, with overall nominal configuration as shown in Fig. 1. The 0-200 Å Fe wedge, 10 Å MgO, and 14 Å Al_2O_3 layers were grown using a dc-sputtering method in the IBM Almaden Research Center, and the wedge extended over ~20 mm, which yields a nominal slope of 10 Å/mm However, it is not essential to know the actual wedge slope precisely, as the wedge scans to be shown later

automatically calibrate a change in z position to the standing wave period. But as rough numbers, the actual experimental wedge scan to be presented below extended over approximately 7.0 mm, and so from the estimate above spanned about 70 Å or about two SW periods. To protect the hydrophilic MgO layer against moisture contamination during transfer of sample in air, the sample was capped with a 14 Å Al_2O_3 layer. The base pressure in the deposition chamber was better than 5×10^{-9} Torr, and the pressure during the sputtering process maintained at 3 mTorr. The MgO and Al_2O_3 layers were formed by reactive sputtering of MgO and Al_2O_3 from a Mg and Al sputter targets, respectively, in an Ar-O_2 environment (97.5%-2.5% mixture for MgO, 93%-7% mixture for Al_2O_3). A small magnetic field (~300 G) was applied along the transverse direction to the Fe wedge during the deposition of Fe layer in order to set uniaxial magnetic anisotropy (easy axis) along the applied field so that the MCD signal in PES becomes optimized along the wedge scan with the given MCD measurement geometry. The experiments were carried out at Beamline 4.0.2 at the Advanced Light Source in LBNL that provides high-brightness tunable circularly polarized photons in the soft x-ray range using an elliptical polarized undulator (EPU) [33]. To set the magnetization in the actual analysis chamber, the sample was magnetized in an applied field of 40G for 120s before the data began to be acquired. The photon energy was set to $h\nu$=900 eV for all measurements, an energy well away from any absorption resonances in the sample. Linear p-polarized light has been used except for the MCD experiments. The size of the focused x-ray beam spot (ca. 100 microns) as compared to the wedge slope of ~200 Å/1 cm = 2 Å/(spot width) is small enough that the standing wave is well defined in vertical distribution and can highlight or suppress the signal from specific depths by tuning the incidence angle to the first-order Bragg reflection of the mirror and scanning the beam along the slope direction of the wedge in the sample (a wedge scan). Several cycles of the SW can thus pass through the sample in a wedge scan. Alternatively, a rocking curve scan of

angle around the multilayer Bragg condition can be used to pass about one half cycle of the SW through the sample. By combining such wedge-scan and rocking curve data with x-ray optical simulations, one can accurately determine the depth profile of each layer, the interdiffusion at the interfaces, and the magnetization at interfaces [28-32], and, as demonstrated for the first time here, the densities of states in interfaces. In particular, by measuring rocking curves and wedge scans of C 1*s* (present in a thin surface contaminant), Al 2*p*, O 1*s* (present in both the Al_2O_3 cap and MgO), Mg 2*p* and Fe 3*p*, and comparing these to theory via an *R*-factor analysis, we can determine the layer concentration profiles. These experimental results are summarized in Fig. 2 and 3(a). Once the layer configuration was characterized by this fitting, wedge scans of both Fe 2*p* MCD and valence-band photoemission were measured at the Bragg angle and these data are presented in Figs. 4 and 3(b), respectively. The former can provide us with the information about depth-resolved Fe magnetization, while the latter permits determining the depth-dependent electronic density of states, particularly near the Fe/MgO interface (as described in more detail below).

III. RESULTS AND DISCUSSION

The core-level photoelectron spectra were fitted in a standard way using Voigt functions with a Shirley background subtraction[34]; all intensities are thus the areas of these Voigt functions above this background. The intensity of the fitted spectra for the rocking curves (Fig. 2) and the wedge scans (Fig. 3(a)) have then been simulated with a specifically designed code taking into account all relevant x-ray optical effects in a dynamical (multiple scattering) formalism, the atomic differential photoelectric cross section, attenuation due to the inelastic mean free paths of the emitted photoelectrons, and photoelectron reflection/refraction at the surface [29-31,35]. The Bragg angle is determined from an analysis of the rocking curve scans in Fig. 2, and found to be 10.2°. Then at this fixed Bragg

angle, the wedge scans were measured. Fig. 3(a) plots the wedge scans recorded for the Al 2*p*, Fe 3*p*, and Mg 2*p* core levels, as well as the valence band. Fig. 3(b) further shows line scans of the valence-band spectra at several key points in the wedge scan: when Fe 3*p* is a maximum, when Mg 2*p* is a maximum, and when the Fe-derived VB intensity near E_F is a minimum; clear differences are noted, depending on whether the Fe-derived density of states near E_F or the deeper densities of states below the band gaps of Al_2O_3 and MgO are being emphasized by the SW position.

Pronounced modulations of both core and valence intensities as high as 45% are clearly seen in both the rocking curve data and via the color scale, also the wedge-scan results, and the wedge-scan data furthermore span about two full cycles of the SW. The forms of the rocking curves are also very different, depending on the depth of a given atomic type from the surface, and the thickness of its parent layer(s). The phases in the core-level wedge-scan data, provide an even more direct depth sensitivity, in that locations of maxima/minima, strongly depend on the atom of origin and its relative depth in the sample (see Fig. 3(a)). The notation "deeper" indicates the direction in which the SW field is moving to greater depths below the surface. The modulation phase as a function of wedge thickness is determined by the location of a given emitting layer with respect to the standing wave multilayer, which fixes the phase of the SW. The wedge distance between two maxima/minima of the intensity modulations corresponds to the standing wave multilayer period or 39.82 Å. For the valence spectra, the intensity modulation phase for the spectral feature near E_F in valence band spectra is well synchronized with that of the Fe 3*p* orbital, consistent with the expectation that the spectral intensity near E_F originates from the metallic Fe layer. By contrast the position of the Mg 2*p* maximum corresponds to a minimum in the Fe-derived intensity, with oxide-derived densities of states being much more important.

In order to more quantitatively map out the entire multilayer depth profile, we have carried out simulations taking into account also interdiffusion (equivalent to roughness in this analysis) between neighboring layers. The optimization of these geometric parameters was done via an *R*-factor analysis, with some of the results being summarized in Figs. 5(a-f). The *R*-factors for intensity are defined as $R\text{-factor (layer)} = \frac{\sum_i \left(I_i^{\exp} - I_i^{\text{cal}} \right)^2}{\sum_i I_i^{\exp\,2}}$. From this analysis we find that the MgO layer is 9 Å thick (very close to its nominal value of 10 Å), while the Al_2O_3 capping layer is 14 Å thick (compared to a nominal 12 Å). The *R*-factor analysis permits estimating errors in these values at ± 2-3 Å, as seen in Fig. 5(c). A small amount of carbon and oxygen buildup is observed on top of the surface, although a slight Ar ion etching has been applied before the experiments. The Fe/MgO and MgO/Al_2O_3 interfaces have been found to be linearly interdiffused over total lengths of 8 Å (~4 ML) and 4 Å (~2 ML), respectively, again with estimated errors of ±2-3 Å, while no interdiffusion was found at the interface between the top C-O contaminant layer and Al_2O_3. Fig. 5(c) indicates one of the two-dimensional R-factor searches that were carried out, here coupling MgO thickness with Fe/MgO interdiffusion (reported as half of the total interdiffusion width).

MCD in Fe 2*p* photoemission was measured with 90% circular polarized light, including a wedge scan, with these results summarized in Fig. 4. These data have been analyzed using the methodology discussed previously for both MCD in standing-wave photoemission [29] and x-ray emission and inelastic scattering [36], with detailed equations appearing in the latter publication. The MCD value is given by $\text{MCD} = (I^+ - I^-)/I^0$ where I^+ (I^-) is the Fe 2*p* peak height for the left (right) polarized light and $I^0 = (I^+ + I^-)/2$. Figs. 3(a,b) show line cuts at a particular position along the wedge corresponding to a wedge thickness of about 44 Å, to illustrate how the MCD is derived. Figs. 4(c,d) show 3D plots of

I^0 and the MCD, respectively, over the full wedge scan. Three peaks in I^0 for the wedge scan are seen (Fig. 4(c)) while three pronounced dips in the MCD signal are also seen shown (Fig. 4(d)). If the magnetization distribution per Fe atom were exactly the same throughout the full Fe layer configuration, the MCD values for the wedge scan would be constant, as discussed previously in connection with standing-wave-excited MCD in Fe Lα x-ray emission [36]. The MCD modulations of more than 50% in our data show that the atom-specific magnetization must vary through the interface. This observation requires an additional parameter to fit the MCD modulation as a function of Fe wedge thickness: the width of the magnetization distribution at the Fe/MgO interface, which we assume in the x-ray optical calculations to be described by a half-gaussian function varying from unity at the pure Fe side of the interface to zero when the Fe has ceased to contribute any net magnetization as sensed by the MCD. A second *R*-factor was then used to fit these data: $R\text{-factor (MCD)} = \frac{\sum_i \left(\text{MCD}_i^{\text{exp}} - \text{MCD}_i^{\text{cal}}\right)^2}{\sum_i \text{MCD}_i^{\text{exp}\,2}}$. Figs. 5(g-h) illustrate the final fit to the MCD data and the R-factor analysis of this fit, in which the parameters are the Fe/MgO interdiffusion width and the half-width-half-maximum of the Gaussian magnetization profile (or 1.17 times its sigma value). The MCD modulation is in fact more sensitive to the Fe/MgO interdiffusion variation than the depth distribution in the layers (cf. Fig. 5(c)), since the MCD modulation is created at the interface only while the core peak intensity modulation originates from both bulk and interfaces. Thereby, we can fit not only the magnetization half width, but also the interdiffusion length more precisely with the MCD modulation results. The *R*-factor 2D contour plots display obvious minima, and we deduced the best fitting parameters from the analysis; a 2.6 Å thick magnetic layer width within the 8.0 Å overall chemical interdiffusion at the Fe/MgO interface. The final results of this analysis of the core-level intensities are shown in Fig. 6 with those for element-specific concentration profiles in 6(a)

and Fe-specific magnetization profiles in 6(b). The MCD results in Fig. 6(b) imply that there exists a magnetic dead layer over the upper 2-3 Å of the Fe/MgO interface (i.e., where the Gaussian profile is reduced to about 10% or less), and one can hypothesize that its chemical composition is likely to be FeO, as we will confirm from the analysis of our valence-band results below.

Finally, we have extracted the matrix-element weighted depth-resolved density of states (DOS) from the Fe/MgO interface region by analyzing the wedge scan of the valence-band spectra shown in the rightmost panel of Fig. 3(a) and in a few line cuts in Fig 3(b). For a given Fe thickness d_{Fe}, the intensity of valence-band photoelectrons emitted with kinetic energy E_{kin} from a depth z can be written as

$$I_{\mathrm{VB}}\left(E_{\mathrm{kin}}, d_{\mathrm{Fe}}\right) = C\int_0^{\infty} \left|\mathrm{E}\left(z, d_{\mathrm{Fe}}\right)\right|^2 \exp\left[-z/\left(\Lambda_e\left(E_{\mathrm{kin}}\right)\sin\theta_e\right)\right]\tilde{D}\left(E_{\mathrm{kin}}, z\right)dz \qquad (1)$$

where C is a constant factor, $\mathrm{E}\left(z, d_{\mathrm{Fe}}\right)$ is the electric field at depth z, $\Lambda_e\left(E_{\mathrm{kin}}\right)$ is the effective attenuation length (EAL) of the photoelectron, θ_e is the photoelectron emission angle with respect to the surface, and $\tilde{D}\left(E_{\mathrm{kin}}, z\right)$ is the matrix-element-weighted DOS at z that we will deduce. The valence-band spans a small region of only about 12 eV out of the ca. 900 eV kinetic energy, so we can evaluate the EALs at the same energy, which yields via the semi-empirical TPP-2M formula the values of 15 Å for Fe, 26 Å for Al_2O_3 and 22 Å for MgO [37]. Since a matrix-element-weighted DOS should be uniform in a uniform layer, Eq. (1) can be rewritten as

$$\begin{aligned} I_{\mathrm{VB}}\left(E_{\mathrm{kin,j}}, d_{\mathrm{Fe}}\right) &\cong C\sum_L \tilde{D}_L\left(E_{\mathrm{kin,j}}\right)\int_{z\in L}\left|\mathrm{E}\left(z, d_{\mathrm{Fe}}\right)\right|^2 \exp\left[-z/\left(\Lambda_{e,L}\sin\theta_e\right)\right]dz \\ &= C\sum_L \tilde{D}_L\left(E_{\mathrm{kin,j}}\right)\int_0^{\infty} W_L\left(z, d_{\mathrm{Fe}}\right)dz \end{aligned} \qquad (2)$$

where $\tilde{D}_L\left(E_{\mathrm{kin,j}}\right)$ is the matrix-element weighted DOS at kinetic energy $E_{\mathrm{kin,j}}$ for a uniform layer L, and W_L is the depth-dependent weighting of a given layer, as given by

$$W_L\left(z,d_{\mathrm{Fe}}\right)\equiv\begin{cases}\left|\vec{E}\left(z,d_{\mathrm{Fe}}\right)\right|^2\exp\left[-z/\left(\Lambda_{e,L}\sin\theta_e\right)\right] & \text{if } z\in L\\ 0 & \text{if } z\notin L\end{cases} \qquad (3)$$

The values of $W_L\left(z,d_{\mathrm{Fe}},E_{\mathrm{kin}}\right)$ are given by the theoretical calculation, with quantitative consideration of the x-ray optics and the photoelectron emission process [35]. We have assumed a total interdiffused interface layer between Fe and MgO of thickness 8.0 Å, as derived from the prior core-level analysis. This leads to four weighting factors $W_{\mathrm{Al_2O_3}}$, W_{MgO}, $W_{\mathrm{Fe/MgO\text{-}interface}}$ and W_{Fe}, which are plotted as a function of z and d_{Fe} in Figs. 7(a-d). The different phases of the SW in the different layers are evident here. Finally, Eq. (2) can be reduced to

$$I_{\mathrm{VB}}\left(E_{\mathrm{kin}},d_{\mathrm{Fe}}\right)\cong C\sum_L\tilde{D}_L\left(E_{\mathrm{kin}}\right)U_L\left(d_{\mathrm{Fe}}\right) \qquad (4)$$

where $U_L\left(d_{\mathrm{Fe}}\right)\equiv\int W_L\left(z,d_{\mathrm{Fe}}\right)dz$, with curves of this integrated quantity being presented in Fig. 7(e). $I_{\mathrm{VB}}\left(E_{\mathrm{kin}},d_{\mathrm{Fe}}\right)$ is given by the Shirley background-subtracted experimental valence-band spectral weight. For a given E_{kin} (or binding energy E_{B}) the number of variables (the number of L's or $\tilde{D}_L's$) to be determined is 4 while the number of equations (the number of d_{Fe}'s) is the total number of valence spectra over the wedge scan, which is 26. Thus, the $\tilde{D}_L$'s can be uniquely determined by solving the over-determined linear Equations (4) in a least-square fit way. An additional constraint on this solution is to require that the $\tilde{D}_L$'s should be zero or positive. The calculations are then straightforward and unambiguous with no parameters to be optimized.

The final calculated matrix-element weighted DOS for each layer $\tilde{D}_{\mathrm{Al_2O_3}}$, $\tilde{D}_{\mathrm{MgO}}$, $\tilde{D}_{\mathrm{Fe/MgO\text{-}interface}}$ and $\tilde{D}_{\mathrm{Fe}}$ are plotted as the solid curves in Fig. 8. Figs. 8(a,b) show that the calculated DOS values for Al_2O_3 and MgO are negligibly small for E_{B} < ~3.9 eV and ~3.5 eV

with respect to E_F, respectively, which correspond to the valence band edges of these insulators. Assuming for simplicity that the Fermi level sits in the middle of the band gap, the values of the valence band edge positions for Al_2O_3 and MgO are close to one half of the band gaps for single crystal samples of these materials, i.e. $E_{gap} \approx 9.5$ eV for Al_2O_3 and $E_{gap} \approx 7.7$ eV for MgO. The small differences may be due to the asymmetry of valence and conduction band edges with respect to the Fermi level, and/or changes in degree of crystallinity. The density of states of the Al_2O_3 layer shows a two-peak structure, with one at ~2.0 eV below the valence-band edge, and one at ~9.4 eV. These features are in reasonable agreement with both XPS data and LDA theory, which exhibit two-main peaks at ~2-3 eV and 7-8 eV below the valence-band edge [38]. Three broad peaks/shoulders are seen in the MgO layer DOS at $E_B \sim 2$, 4, and 7 eV below the valence-band edge (see Fig. 8(b)). These three features are also observed in previous work on MgO deposited on Fe, at very nearly the same binding energies [39]. The results for both Al_2O_3 and MgO thus confirm that our approach for extracting DOSs is reasonable and quantitative. For the Fe layer minus the interface, the DOS is shown in Fig. 8(d); here, we find a pronounced peak observed near E_F followed by a shoulder at E_B ~2.0 eV, and a broad, weak feature at about 6 eV that are also confirmed by previous XPS experiments on bulk Fe films [40] and MgO films grown on Fe single crystals [39]. Finally, the Fe/MgO interdiffused interface layer exhibits a distinctly different DOS compared to that of the MgO and Fe layers. The DOS shows a high spectral weight at E_F and a peak very near that of the Fe layer, but also a broad but pronounced feature is observed at $E_B \sim 3$-5 eV, in addition to a peak near E_F. Since our model assumes a linear interdiffusion at the Fe/MgO interface, the peak at E_F may originate from that portion of the Fe/MgO interdiffused interface closest to Fe. Assuming that the interdiffused region is stoichiometric, the most probable Fe-O chemical composition ratio is FeO to satisfy the two observations above. This is reasonable, since prior photoemission shows a strong Fe-derived

features at ~2, 4, and 7 eV below the VB maximum [41]. FeO is a paramagnetic metal at room temperature and becomes antiferromagnetic below T~190 K [42]. Therefore, a thin nonmagnetic metallic layer, FeO, formed at the Fe/MgO interface can result in a significant reduction of the spin-dependent tunneling, which may account for the discrepancy between experiment and the theoretical prediction of the TMR values. On a microscopic scale, we can cite three possible sources of this discrepancy: that the presence an interface layer that is at least partially FeO destroys proper wave function matching at the interface, that the paramagnetic nature of this FeO reduces spin-dependent tunneling, and that the metallic nature of the FeO/MgO interface reduces the effectiveness of tunneling. Our data do not permit deciding conclusively among these, however.

As a final step in our analysis of the valence-band data, we have also calculated the DOSs neglecting the Fe/MgO interdiffused region, and these results are plotted in dotted lines in Figs. 8(a,b) and (d). As might be expected, the DOSs and valence band edges of the Al_2O_3 and Fe layers do not change significantly by this consideration. However, the DOS for the MgO layer becomes significantly different over E_B ~ 1- 6 eV from the case that treated the valence-band region separately, showing a valence band edge at ~1.3 eV below E_F (see Fig. 8(c)). This is remarkable in that 1.3 eV is in fact close to the barrier height value estimated from I-V tunneling transport measurements of MTJs based on MgO barriers [43], and this may suggest that the injected spins from the Fe layer pass through an effectively lowered barrier height due to the interdiffusion at the interfaces.

Finally, we note that our conclusions are for a sample that was grown by reactive sputtering, with the MgO formed by simultaneous oxidation of a Mg layer during its deposition. Thus, the Fe and Mg layers were not epitaxial in nature, and some oxidation of Fe might be expected, although the MgO is expected to be highly textured. By comparison, a recent study of the Fe/MgO system using the SWEDGE method by our group was based on

samples grown on a similar Mo/Si multilayer, but with the MgO evaporated directly and not involving oxidation of deposited Mg. These measurements were also carried out with much higher photon energies of 2.01 and 4.00 keV, and thus up to about three times higher electron effective attenuation lengths (EALs), which would lead to less sensitivity to the Fe/MgO. Nonetheless, the analysis of this data yields about the same conclusion concerning Fe/MgO interdiffusion (~6 Å compared to the ~8 Å found here). However, there is no evidence of oxide formation at the interface, probably due to the difference method of MgO formation. This study was more limited than the present one, in that no MCD measurements were made, no analysis such as that of Eq. 4 was performed, and the much larger EALs involved would in any case make it more difficult to clearly resolve the DOS near the interface**.**

IV. CONCLUSIONS

In summary, we have used a powerful new tool, standing-wave photoemission including the SWEDGE method, to explore the depth-dependent chemical, magnetic and electronic structures of a prototypical MTJ sample by measuring the core-level photoemission, core-level MCD and valence-band photoemission. The combination of experiment and x-ray optical calculations shows that the Fe/MgO interface is compositionally interdiffused over an 8 Å thick region and that the magnetization (at room temperature) decays with a halfwidth of about 2.6 Å deep into the interdiffused interface, indicating via the guassian curve of Fig. 6(b) a more or less dead layer of 2-3 Å thick near the top of the interface. We have also deduced the layer-resolved DOS's including this interface region and found that the MgO layer has a valence band edge at E_B ~ 3.5 eV and the interdiffused layer appears to be FeO-like, and thus non-magnetic and metallic. On the other hand, the MgO valence band edge decreases to 1.3 eV when the interdiffused region is not considered separately in the analysis, providing a link to transport measurement determinations of this

quantity. This work thus helps to resolve several controversies over the discrepancy between magnetotransport measurements and other characterization experiments on MgO-based MTJs.

Acknowledgements

BB and CP gratefully acknowledge the support through the Feodor-Lynen fellowship of the Humboldt foundation. CF also acknowledges support of the Helmholtz Association and the Humboldt Foundation. Additionally, the experiments at the ALS and the participation of LBNL Materials Sciences Division scientists were supported by DOE Contract No DE-AC02-05CH11231.

Figure Captions

Figure 1. Schematic diagram of our sample, with the Fe in a wedge layer, and including the geometry of the exciting x-ray beam and outgoing photoelectrons. Reflection from the Si/Mo multilayer mirror, with light incident at the first-order Bragg incidence angle of about 10.2°, creates a strong standing wave above the mirror, as qualitatively indicated. The magnetic easy axis for Fe layer is in-plane and the sample has been magnetized perpendicular to the wedge direction and thus nearly collinear to the incidence direction of the light, as required for the MCD measurements.

Figure 2. Rocking curves of O 1*s*, C 1*s*, Al 2*p*, Fe 3*p* and Mg 2*p* orbital photoemission intensities with excitation energy $h\nu$=900 eV near the Bragg angle measured at the center of samples (corresponding to ~ 100 Å MgO thickness in wedge). This measurement determines the Bragg angle (=10.2°).

Figure 3. (a) 2D plots of the wedge scans of photoelectron spectra for Al 2*p* (left panel), Fe 3*p* and Mg 2*p* (middle panel) and the valence band (right panel). The color code is violet: high intensity, yellow: low intensity, with a color scale as inset. (b) Line cuts through the valence-band data of Fig. 2(b) at several key points emphasizing maximum and minimum Fe emission, as well as maximum MgO emission, as judged from the core-level data.

Figure 4. Line cuts of Fe 2*p* MCD results at a certain point along a wedge scan, at approximately an Fe thickness of ~44 Å (a) Raw intensities using left (I^+) and right (I^-) circular polarized light, and (b) normalized MCD signal derived from the data in (a), where $I^0 = (I^+ + I^-)/ 2$. 3D plots of (c) the whole series of I^0 intensity measurements taken in the wedge scan of the Fe 2*p* core level, and (d) the MCD signal derived from (c).

Figure 5. The final best fits of x-ray optical theory to the experimental wedge scan data for both core-level intensities ((a) Fe 3*p*, (b) Mg 2*p*, (d) Al 2*p*, (e) O 1*s*, and (f) C 1*s* and Fe 2*p* MCD (g). Also shown are sample *R*-factor plots (among several that were done) indicating the two-parameter sensitivity to (c) the intensity analysis of interdiffusion at the Fe/MgO interface and the MgO thickness, and (h) the MCD analysis as a function of the Fe/MgO interdiffusion and the Gaussian magnetization half-width at half-maximum.

Figure 6. Final results for the (a) the assumed linear concentration profile in the sample, including interdiffusion at all interfaces and (b) the assumed half-Gaussian atom-specific Fe magnetization across the Fe/MgO interface.

Figure 7. (a)-(d) 2D plots of the depth-resolved theoretical weighting factors W_L for each layer, as defined in Eq. (3), as a function of Fe wedge thickness d_{Fe} and depth z, for: (a) $W_{\mathrm{Al_2O_3}}$, (b) W_{MgO}, (c) $W_{\mathrm{Fe/MgO\text{-}interface}}$ and (d) W_{Fe}. Note that these include both the variation of the electric field as the standing wave scans through the sample and the inelastic attenuation of the escaping photoelectrons. With the higher photon energies of 2-4 keV used in a similar SWEDGE study in ref. [44], the attenuation of the photoelectron intensity in each layer with z would be 2-3 times less (i.e. EALs would be 2-3 times larger). (d) The integrals U_L of W_L over a given layer, $U_{\mathrm{Al_2O_3}}$ (black), U_{MgO} (red), $U_{\mathrm{Fe/MgO\text{-}interface}}$ (green) and U_{Fe} (blue) are plotted versus depth.

Figure 8. The final least-squares fitted matrix-element weighted layer DOS's derived from Eq. that considers the Fe/MgO interdiffused interface layer separately are shown in thick solid curves for (a) Al_2O_3 layer (black), (b) MgO layer (red), (c) Fe/MgO interface layer

(green) and (d) the Fe layer below the interface (blue). Also shown as dotted curves in the same colors for (a) Al_2O_3 layer, (b) MgO layer and (d) Fe layer are calculated DOSs that do not take into account the interdiffused layer separately. The valence band edges for insulating layers are indicated by dashed lines for (a) the Al_2O_3 layer and (b) the MgO layer (solid with inclusion of the interface and dashed without it).

REFERENCES

1. T. Miyazaki and N. Tezuka, J. Magn. Magn. Mat. **139**, L231 (1995).
2. J. S. Moodera, L. R. Kinder, T. M. Wong, and R. Meservey, Phys. Rev. Lett. **74**, 3273 (1995).
3. X.-F. Han, T. Daibou, M. Kamijo, K. Yaoita, H. Kubota, Y. Ando, and T. Miyazaki, Jpn. J. Appl. Phys. **39**, L439 (2000).
4. S. S. P. Parkin, K. P. Roche, M. G. Samant, P. M. Rice, R. B. Beyers, R. E. Scheuerlein, E. J. O'Sullivan, S. L. Brown, J. Bucchigano, D. W. Abraham, Yu Lu, M. Rooks, P. L. Trouilloud, R. A. Wanner, and W. J. Gallagher J. Appl. Phys. **85**, 5828 (1999).
5. M. Julliere, Phys. Lett. A **54**, 225 (1975).
6. W. H. Butler, X. G. Zhang, T. C. Schulthess, and J. M. MacLaren, Phys. Rev. B **63**, 054416 (2001).
7. J. Mathon and A. Umerski, Phys. Rev. B **63**, 220403 (2001).
8. S. S. P. Parkin, C. Kaiser, A. Panchula, P. M. Rice, B. Hughes, M. Samant, and S.-H. Yang, Nature Mater. **3**, 862-867 (2004).
9. S. Yuasa, T. Nagahama, A. Fukushima, Y. Suzuki, and K. Ando, Nature Mater. **3**, 868-871 (2004).
10. C. Bellouard, J. Faure-Vincent, C. Tiusan, F. Montaigne, M. Hehn, V. Leiner, H. Fritzsche, and M. Gierlings, Phys. Rev. B **78**, 134429 (2008).
11. F. Greullet, C. Tiusan, F. Montaigne, M. Hehn, D. Halley, O. Bengone, M. Bowen, and W. Weber, Phys. Rev. Lett. **99**, 187202 (2007).
12. D. Halley, O. Bengone, S. Boukari, and W. Weber, Phys. Rev. Lett. **102**, 027201 (2009).

13. M. Klaua, D. Ullmann, J. Barthel, W. Wulfhekel, J. Kirschner, R. Urban, T. L. Monchesky, A. Enders, J. F. Cochran, and B. Heinrich, Phys. Rev. B **64**, 134411 (2001).
14. Yan Li, Y. Chye, Y. F. Chiang, K. Pi, W. H. Wang, J. M. Stephens, S. Mack, D. D. Awschalom, and R. K. Kawakami, Phys. Rev. Lett. **100**, 237205 (2008).
15. P. Luches, S. Benedetti, M. Liberati, F. Boscherinic, I.I. Pronind and S. Valeri, Surface Science **583**, 191-198 (2005).
16. H. L. Meyerheim, R. Popescu, N. Jedrecy, M. Vedpathak, M. Sauvage-Simkin, R. Pinchaux, B. Heinrich, and J. Kirschner, Phys. Rev. B **65**, 144433 (2002).
17. H. L. Meyerheim, R. Popescu, J. Kirschner, N. Jedrecy, M. Sauvage-Simkin, B. Heinrich, and R. Pinchaux, Phys. Rev. Lett. **87**, 076102 (2001).
18. G. X. Miao, Y. J. Park, J. S. Moodera, M. Seibt, G. Eilers, and M. Münzenberg, Phys. Rev. Lett. **100**, 246803 (2008).
19. T. Niizeki, N. Tezuka, and K. Inomata, Phys. Rev. Lett. **100**, 047207 (2008).
20. C. Tiusan, J. Faure-Vincent, C. Bellouard, M. Hehn, E. Jouguelet, and A. Schuhl, Phys. Rev. Lett. **93**, 106602 (2004).
21. C. Tusche, H. L. Meyerheim, N. Jedrecy, G. Renaud, and J. Kirschner, Phys. Rev. B **74**, 195422 (2006).
22. K. D. Belashchenko, J. Velev, and E. Y. Tsymbal, Phys. Rev. B **72**, 140404 (2005).
23. C. Heiliger, M. Gradhand, P. Zahn, and I. Mertig, Phys. Rev. Lett. **99**, 066804 (2007).
24. C. Heiliger and M. D. Stiles, Phys. Rev. Lett. **100**, 186805 (2008).
25. C. Heiliger, P. Zahn, B. Y. Yavorsky, and I. Mertig, Phys. Rev. B **73**, 214441 (2006).
26. L. Plucinski, Y. Zhao, B. Sinkovic, and E. Vescovo, Phys. Rev. B **75**, 214411 (2007).
27. F. Matthes, L. N. Tong, and C. M. Schneider, J. Appl. Phys. **95**, 7240 (2004).

28. S.-H. Yang, B. S. Mun, A. W. Kay, S.-K. Kim, J. B. Kortright, J. H. Underwood, Z. Hussain, and C. S. Fadley, Surf. Sci. **461**, L557 (2000).
29. S.-H. Yang, B. S. Mun, N. Mannella, S.-K. Kim, J. B Kortright, J. Underwood, F. Salmassi, E. Arenholz, A. Young, Z. Hussain, M. A Van Hove, and C. S Fadley, J. Phys.: Condens. Matter **14**, L407 (2002).
30. S.-H. Yang, B. S. Mun, N. Mannella, A. Nambu, B. C. Sell, S. B. Ritchey, F. Salmassi, A. Shick, S. S. P. Parkin. and C. S. Fadley, J. Phys.: Condens. Matter **18**, L259 (2006).
31. S.-H. Yang, B. C. Sell, and C. S. Fadley, J. Appl. Phys. **103**, 07C519 (2008).
32. A. X. Gray, C. Papp, B. Balke, S.-H. Yang, M. Huijben, E. Rotenberg, A. Bostwick, S. Ueda, Y. Yamashita, K. Kobayashi, E. M. Gullikson, J. B. Kortright, F. M. F. DeGroot, G. Rijnders, D. H. A. Blank, R. Ramesh, and C. S. Fadley, Phys. Rev. B **82**, 205116 (2010).
33. A. T. Young, V. Martynov, and H. A. Padmore, J. Electron Spectrosc. Rel. Phenom. **101–103**, 885–889 (1999).
34. D. A. Shirley, Phys. Rev. B 5, 4709 (1974).
35. S.-H. Yang, A. X. Gray, A. X. Kaiser, B. S. Mun, B. C. Sell, and C. S. Fadley, Program for calculating soft X-ray optical effects with strong reflectivity in x-ray photoemission and x-ray emission, *discussed in*. "X-ray Optics, Standing Waves, and Interatomic Effects in Photoemission and X-ray Emission", C. S. Fadley, S.-H. Yang, B. S. Mun, J. Garcia de Abajo, Chapter in the book "Solid-State Photoemission and Related Methods: Theory and Experiment", W. Schattke and M.A. Van Hove, Editors, (Wiley-VCH Verlag, Berlin GmbH, 2003), ISBN: 3527403345.

36. B. C. Sell, S. B. Ritchey, S.-H. Yang, S. S. P. Parkin, M. Watanabe, B. S. Mun, L. Plucinski, N. Mannella, A. Nambu, J. Guo, M. W. West, F. Salmassi, J. B. Kortright, and C. S. Fadley, J. Appl. Phys. **103**, 083515 (2008).
37. S. Tanuma, C. J. Powell, and D. R. Penn, Surf. Interface Anal. **43**, 689 (2011); S. Tougaard, QUASES-IMFP-TPP2M™ Software Package - Ver.2.1, available at: http://www.quases.com .
38. S.-D. Mo, Y.-N. Xu, and W. Y. Ching, J. Am. Ceram. Soc. **80**, 1193–1197 (1997); J. A. Rotole and P. M. A. Sherwood, Surface Science Spectra **5**, 11 (1998) and 5, 18 (1998).
39. M. Sicot, S. Andrieu, P. Turban, Y. Fagot-Revurat, H. Cercellier, A. Tagliaferri, C. De Nadai, N. B. Brookes, F. Bertran, and F. Fortuna, Phys. Rev. B **68**, 184406 (2003).
40. A. N. Mansour and R. A. Brizzolara, Surface Science Spectra **4**, 197 (1997).
41. F. Parmigiani and L. Sangaletti, J. Electron Spectrosc. Rel. Phenom. **98-99**, 287 (1999).
42. Landolt Börnstein, Substance / Property Index, New Series III/27g, 6.1.2.1 Simple monoxides MO: http://www.springermaterials.com/docs/pdf/10201470_28.html.
43. P. G. Mather, J. C. Read, and R. A. Buhrman, Phys. Rev. B **73**, 205412 (2006).
44. S. Döring, F. Schönbohm, U. Berges, R. Schreiber, D. E. Bürgler, C. M. Schneider, M. Gorgoi, F. Schäfers, C. Papp, B. Balke, C. S. Fadley, and C. Westphal, Phys. Rev. B 83, 165444 (2011).

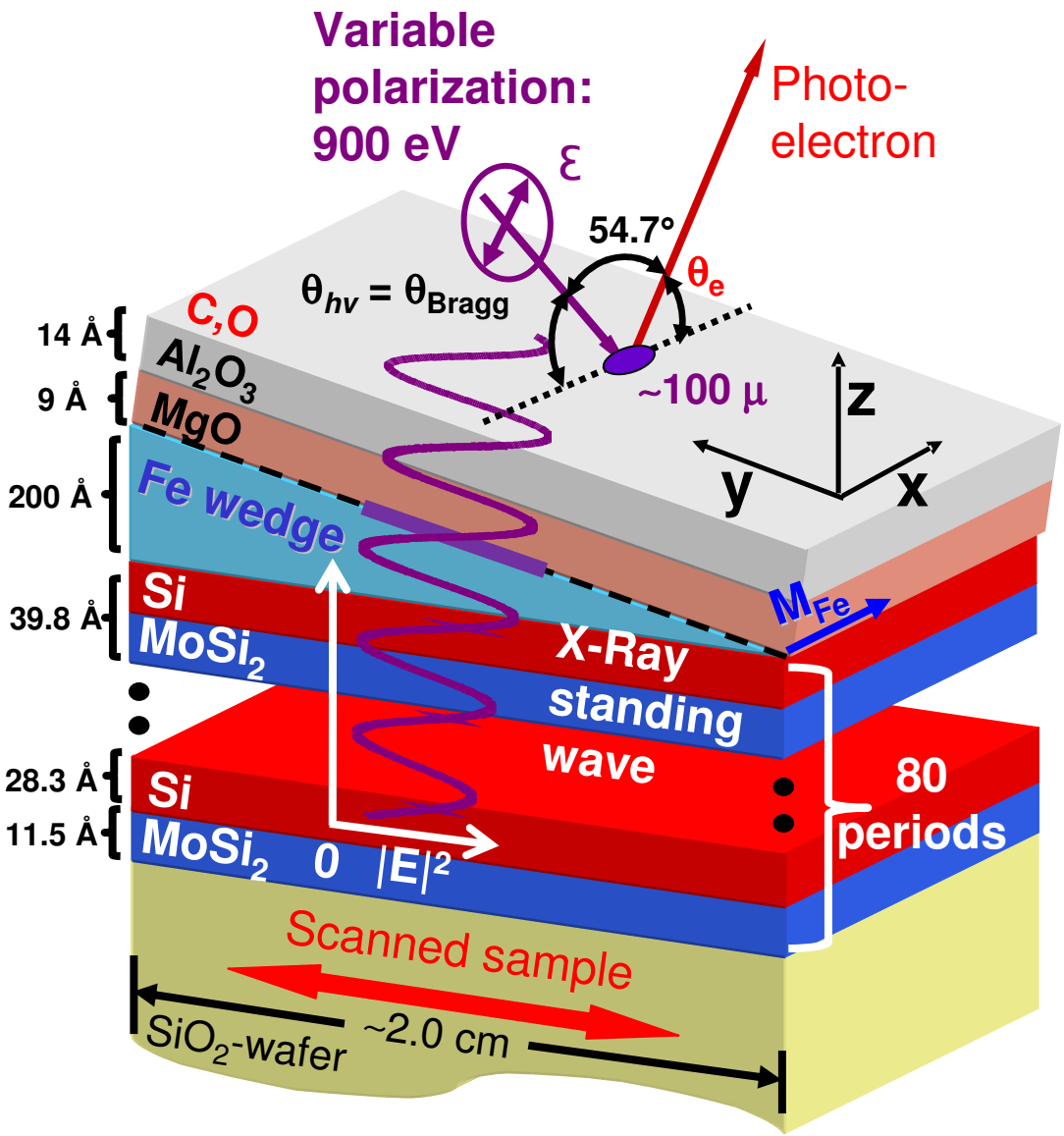
Variable
polarization:
900 eV
ε
Photo-
electron
54.7°
θe
θhv = θBragg
C,O
14 Å
Al2O3
9 Å
MgO
200 Å
Fe wedge
~100 μ
z
y
x
Si
39.8 Å
MoSi2
MFe
X-Ray
standing
wave
80
periods
28.3 Å
Si
11.5 Å
MoSi2
0
|E|2
Scanned sample
SiO2-wafer
~2.0 cm

Figure 1

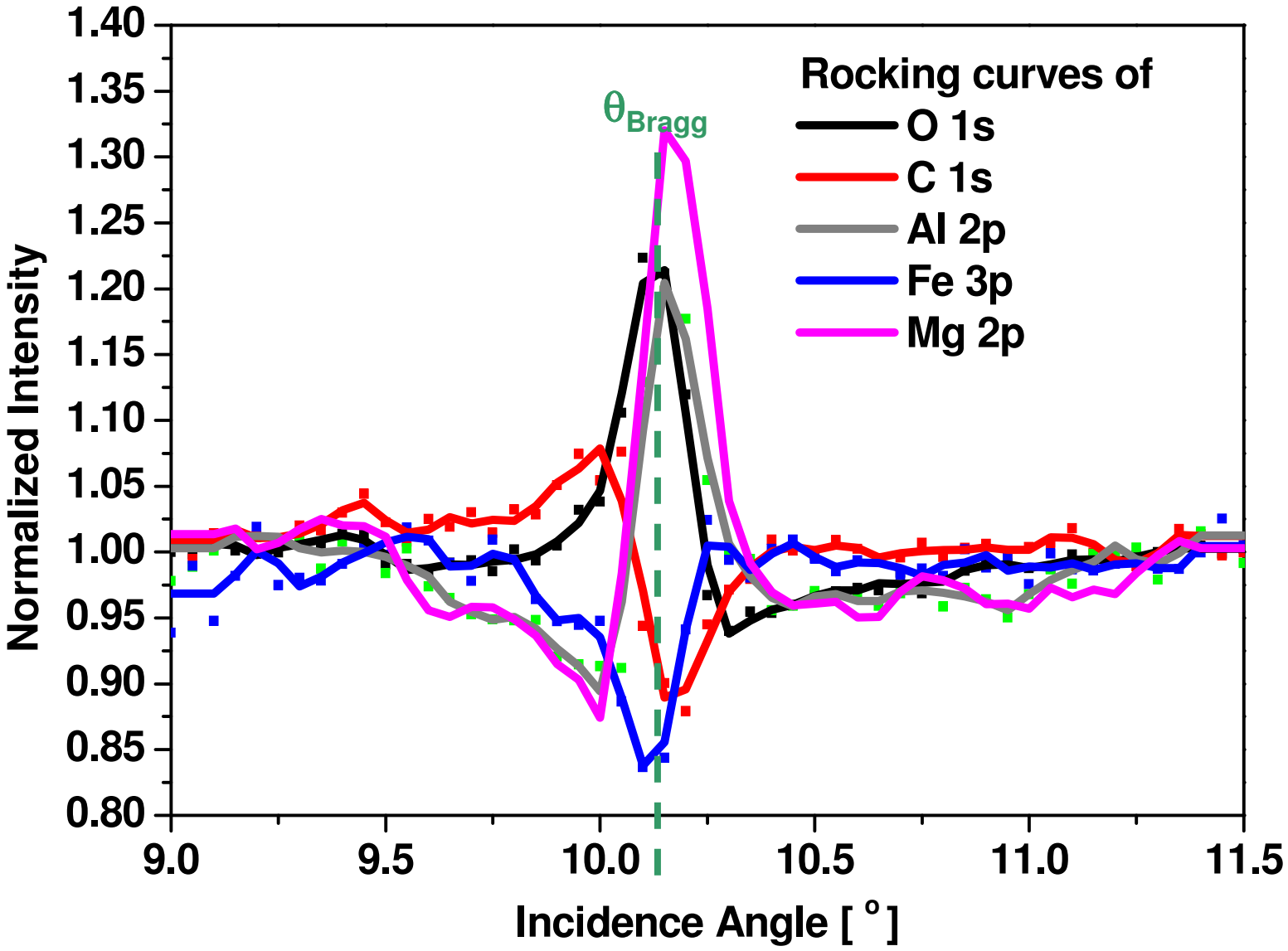
Normalized Intensity
1.40
1.35
1.30
1.25
1.20
1.15
1.10
1.05
1.00
0.95
0.90
0.85
0.80
9.0
9.5
10.0
10.5
11.0
11.5
Incidence Angle [°]
θBragg
Rocking curves of
O 1s
C 1s
Al 2p
Fe 3p
Mg 2p

Figure 2

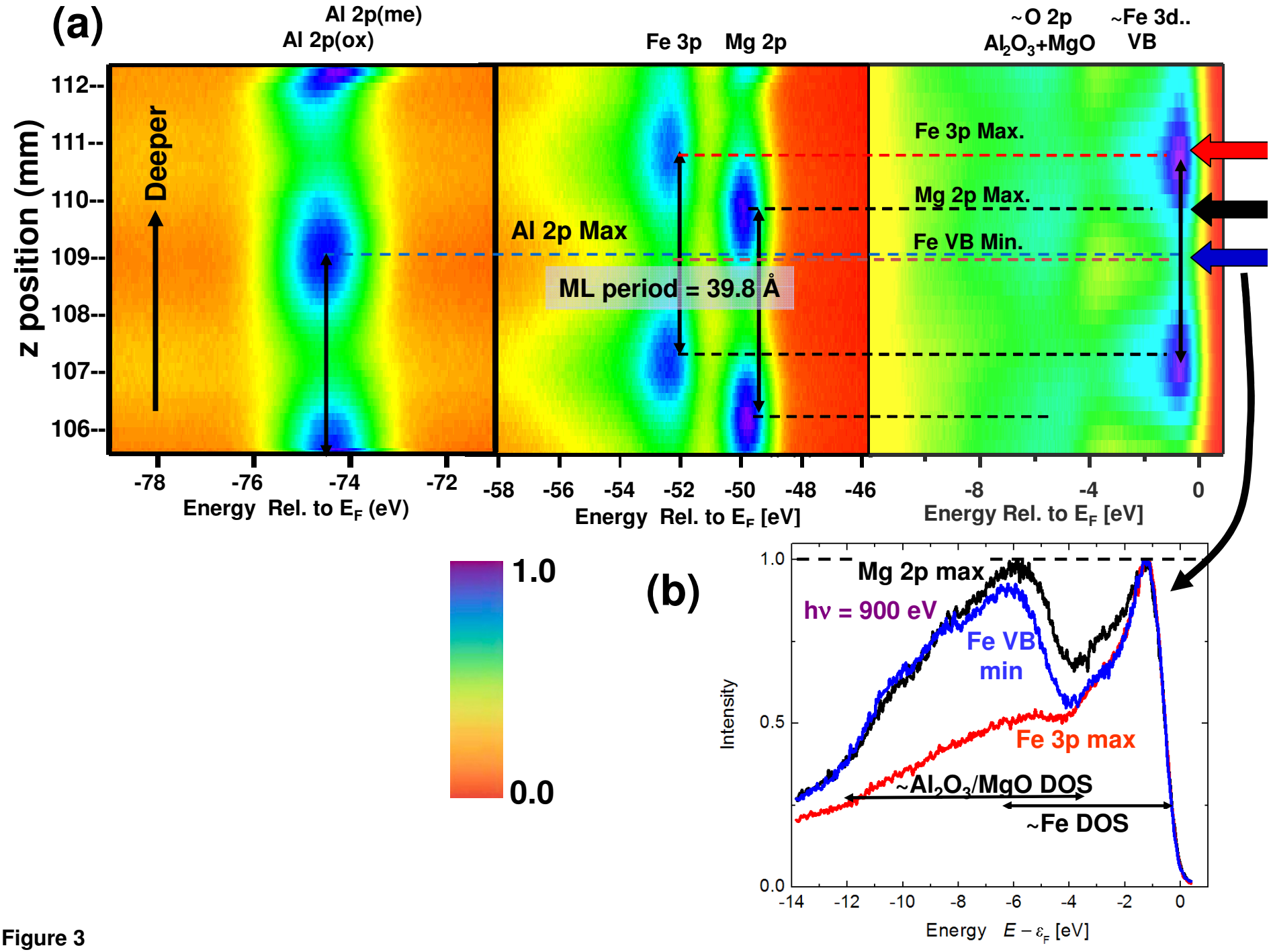
(a)
Al 2p(me)
Al 2p(ox)
Fe 3p
Mg 2p
~O 2p
Al2O3+MgO
~Fe 3d..
VB
z position (mm)
112--
111--
110--
109--
108--
107--
106--
Deeper
Al 2p Max
Fe 3p Max.
Mg 2p Max.
Fe VB Min.
ML period = 39.8 Å
-78
-76
-74
-72
Energy Rel. to EF (eV)
-58
-56
-54
-52
-50
-48
-46
Energy Rel. to EF [eV]
-8
-4
0
Energy Rel. to EF [eV]
1.0
0.0
(b)
Mg 2p max
hν = 900 eV
Fe VB min
Fe 3p max
~Al2O3/MgO DOS
~Fe DOS
Intensity
1.0
0.5
0.0
-14
-12
-10
-8
-6
-4
-2
0
Energy E − εF [eV]

Figure 3

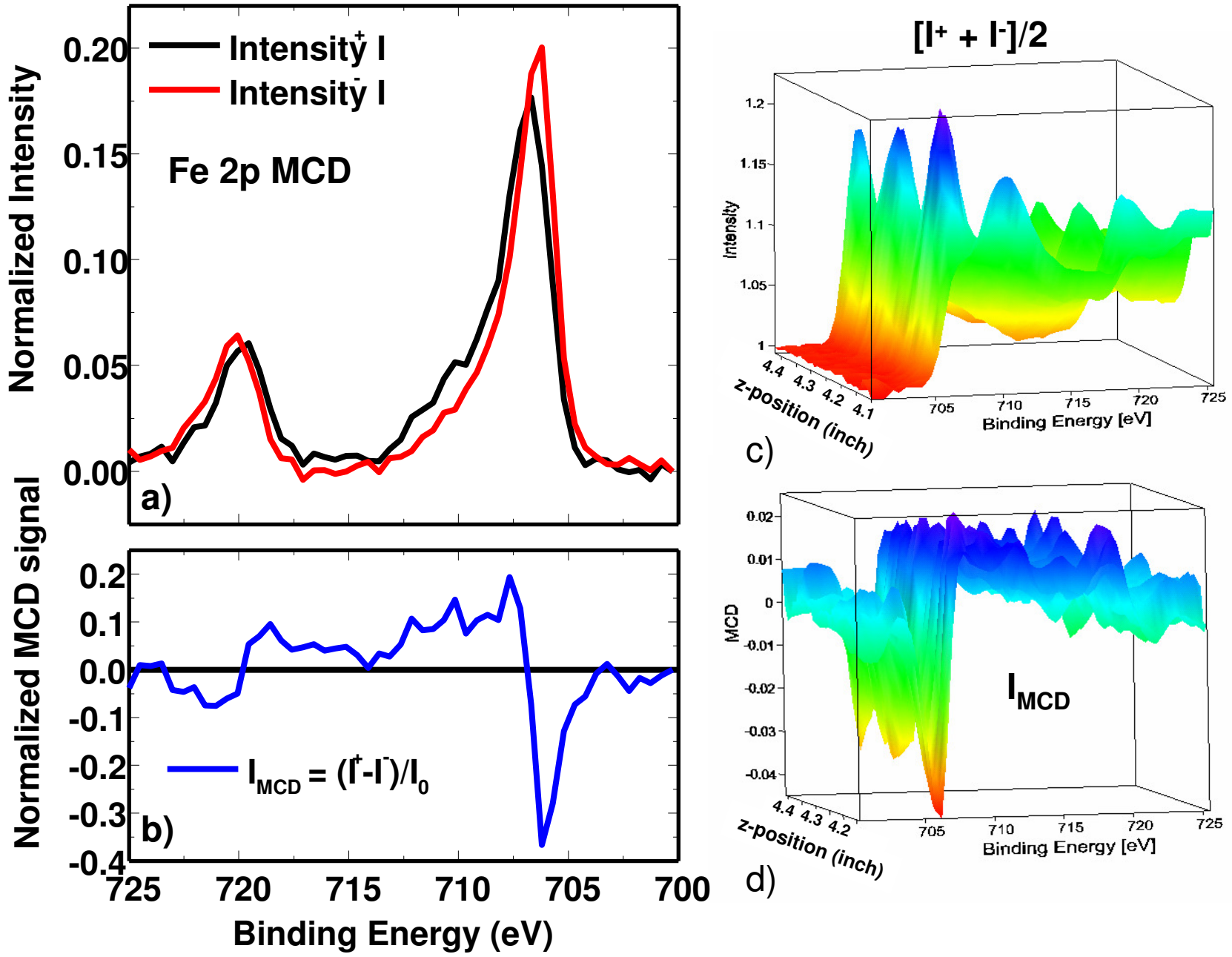
Normalized Intensity
Intensity I+
Intensity I-
Fe 2p MCD
a)
Normalized MCD signal
I_MCD = (I+-I-)/I0
b)
Binding Energy (eV)
[I+ + I-]/2
Intensity
z-position (inch)
Binding Energy [eV]
c)
MCD
I_MCD
z-position (inch)
Binding Energy [eV]
d)

Figure 4

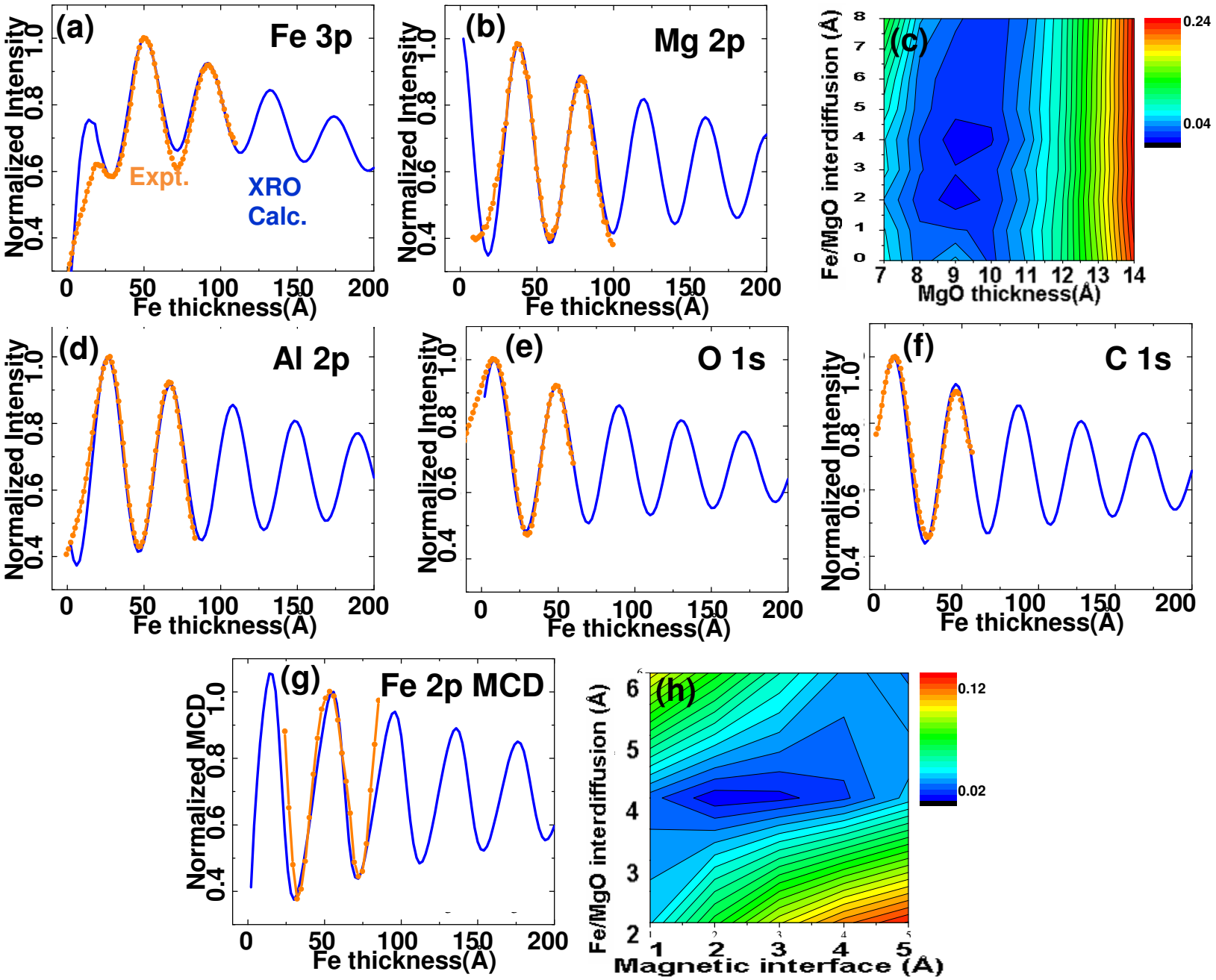
(a)
Fe 3p
Expt.
XRO
Calc.
Normalized Intensity
Fe thickness(Å)
(b)
Mg 2p
(c)
Fe/MgO interdiffusion (Å)
MgO thickness(Å)
0.24
0.04
(d)
Al 2p
(e)
O 1s
(f)
C 1s
(g)
Fe 2p MCD
Normalized MCD
(h)
Magnetic interface (Å)
0.12
0.02

Figure 5

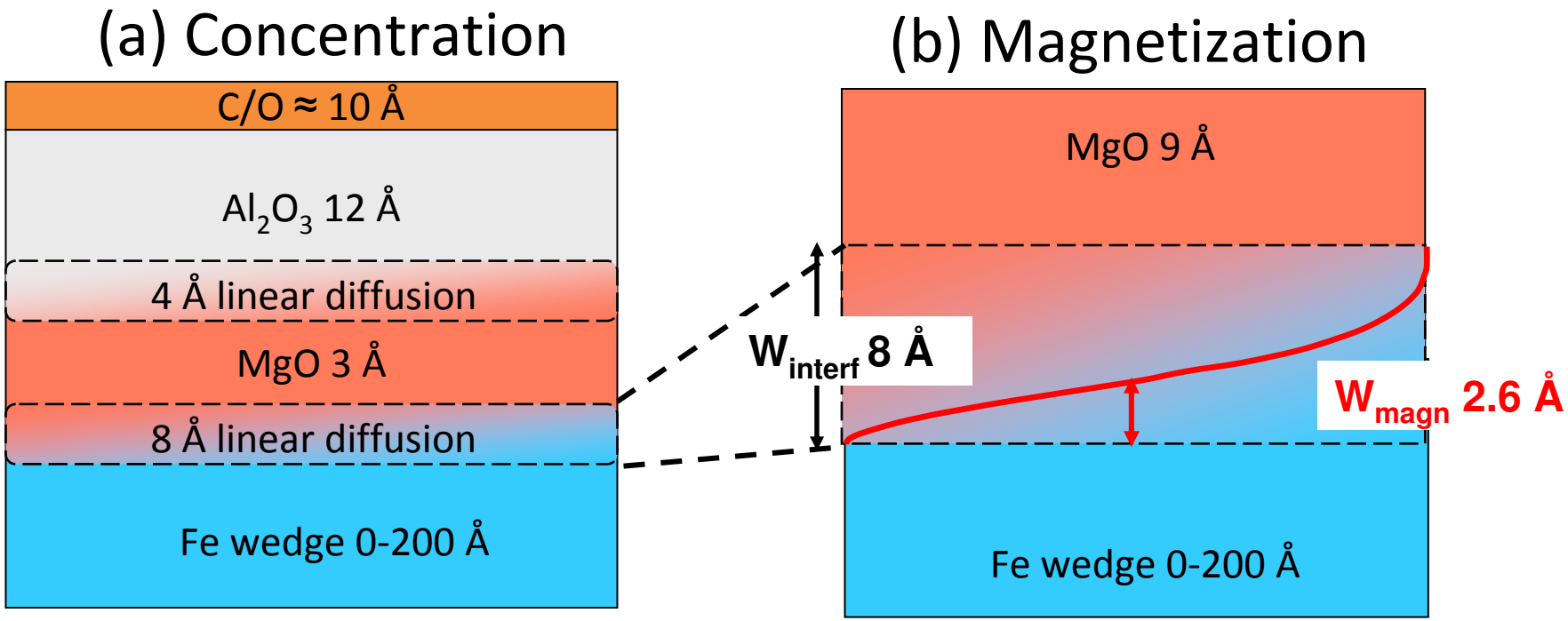
(a) Concentration
C/O ≈ 10 Å
Al2O3 12 Å
4 Å linear diffusion
MgO 3 Å
8 Å linear diffusion
Fe wedge 0-200 Å
(b) Magnetization
MgO 9 Å
Winterf 8 Å
Wmagn 2.6 Å
Fe wedge 0-200 Å

Figure 6

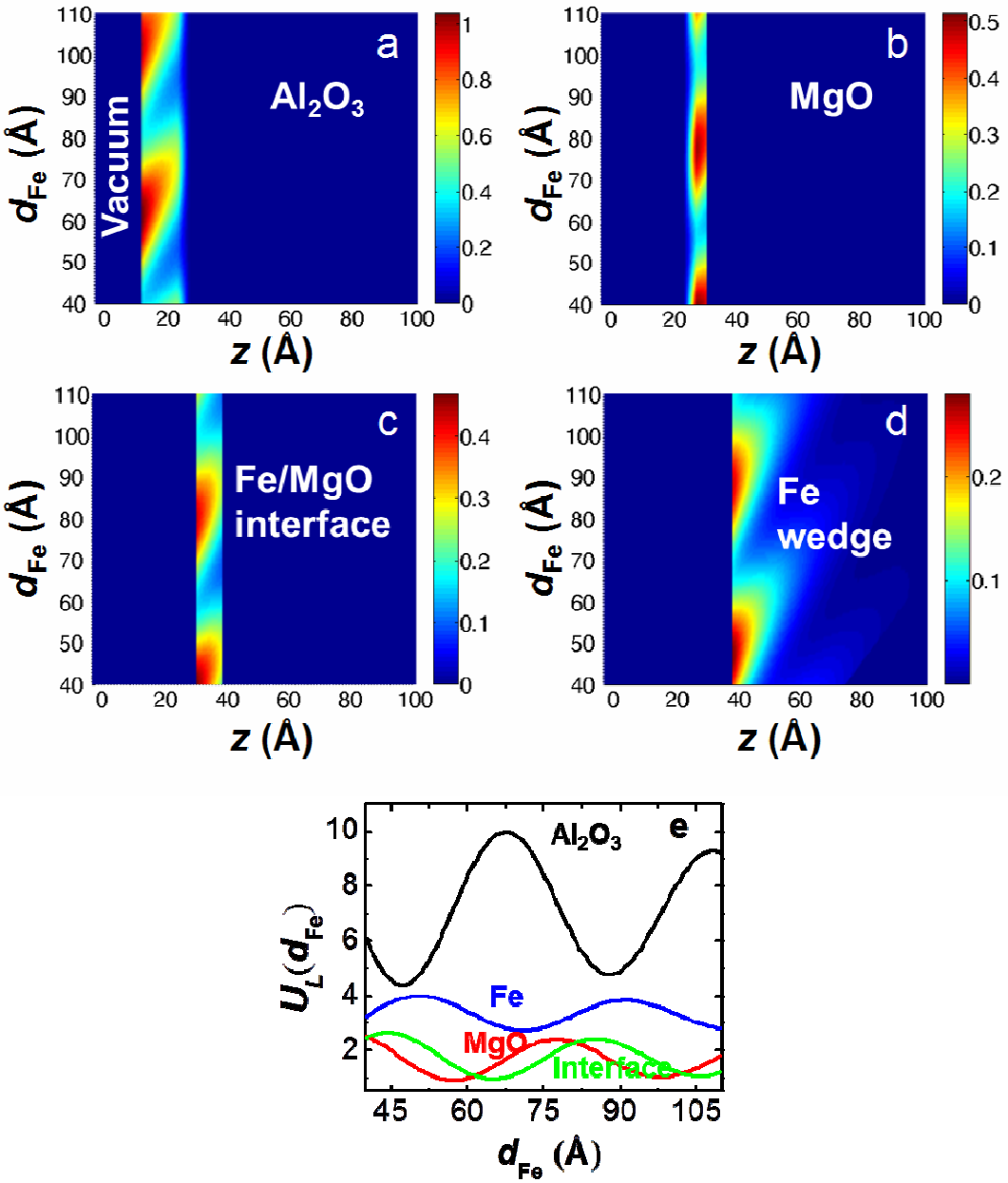
a
Vacuum
Al_2O_3
b
MgO
c
Fe/MgO
interface
d
Fe
wedge
d_{Fe} (Å)
z (Å)
e
Al_2O_3
Fe
MgO
Interface
$U_L(d_{Fe})$
d_{Fe} (Å)

Figure 7

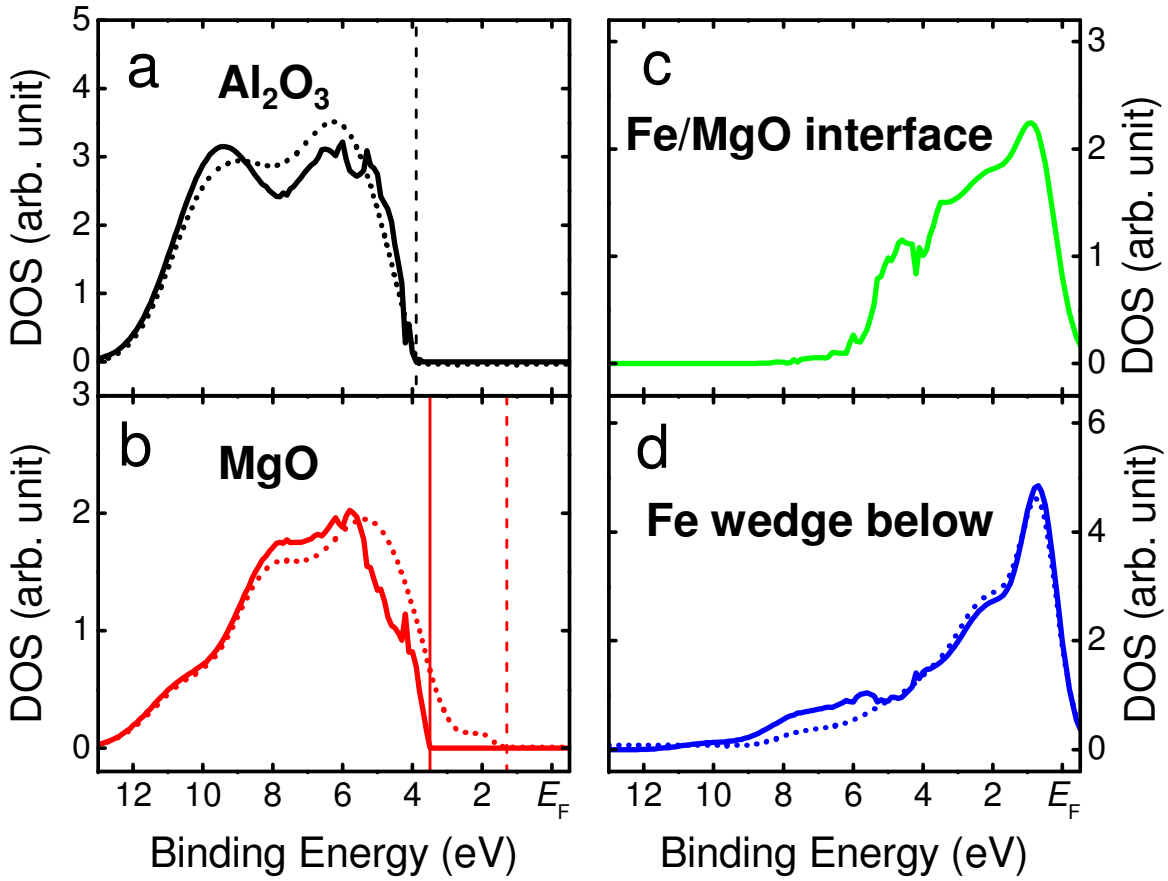
a
Al_2O_3
b
MgO
c
Fe/MgO interface
d
Fe wedge below
DOS (arb. unit)
DOS (arb. unit)
DOS (arb. unit)
DOS (arb. unit)
12 10 8 6 4 2 E_F
12 10 8 6 4 2 E_F
Binding Energy (eV)
Binding Energy (eV)

Figure 8